Available online at www.sciencedirect.com
SCIENCE DIRECT®
ELSEVIER
International Journal of Heat and Mass Transfer 47 (2004) 4019–4029
International Journal of HEAT and MASS TRANSFER
www.elsevier.com/locate/ijhmt

# Plasma energy transport to an electrically biased surface

F.B. Yeh [a,*], P.S. Wei [b,1]

[a] Department of Marine Mechanical Engineering, Chinese Naval Academy, Kaohsiung, Taiwan, ROC
[b] Department of Mechanical and Electro-Mechanical Engineering, National Sun Yat-Sen University, Kaohsiung, Taiwan, ROC

Received 29 March 2004; received in revised form 2 June 2004

## Abstract

The total energy flux, including ion and electron energy fluxes, transport to a biased surface in contact with a plasma is systematically and analytically investigated in this study. Micro-electro-mechanical systems (MEMS), semiconductor technology, plasma etching, spray deposition, sputtering, cutting and surface treatment, etc. are usually controlled by energy transfer from the plasma to workpiece. In this work, the plasma is composed of a collisionless presheath and sheath on an electrically negative biased workpiece partially reflecting and secondly emitting ions and electrons. The presheath is an ionization region that continuously produces ions to supply ion loss to the surface, while the sheath is a space-charge region that accelerates ions and retards electrons toward the surface. Based on the kinetic analysis, the predicted ion density, velocity and energy transmission factor on the surface are found to agree well with experimental data. The effects of dimensionless ion recombination and electron absorption energies, reflectivities and second emissivities of the ions and electrons on the wall, ion-to-electron mass ratio, charge number, electron-to-ion source temperature ratio at the presheath edge, and net current density on energy fluxes across the sheath are obtained. Energies released from recombination of the ions and electrons on the surface play the most important role in energy transfer to the workpiece. The sheath should be accounted for predicting energy transport to a biased surface.
© 2004 Elsevier Ltd. All rights reserved.

*Keywords:* Plasma energy flux; Sheath; Presheath; Net current density; Energy transmission factor; Biased surface

## 1. Introduction

Micro-electro-mechanical systems (MEMS), semiconductor technology, plasma etching, spray deposition, sputtering, cutting and surface treatment of plasma processing, designing divertors and limiters in nuclear fusion and probe devices, etc., are closely related to energy transfer from the plasma to the surface. In contrast to energy transfer from neutral and ordinary gases, the energy flux from the plasma to the workpiece surface is controlled by sheath voltage in front of the surface. Since mobilities of ions and electrons are different, the plasma exhibits net positive charges with respect to the surface [1]. Debye shielding confines the negative potential to a thin layer called the sheath or space-charge region in a thickness of around several Debye lengths in front of the wall. The electrons thus are repelled and the ions are accelerated by the negative wall potential. An ionization region or presheath supplies the ions lost to the wall. Small electrostatic potential in the presheath accelerates the ions up to sonic speed before entering the sheath, as first explicitly pointed out by Bohm [2]. The surface therefore acts as particle and energy sinks for the plasma.

Several plasma-based techniques may be employed to control energy and mass fluxes of the ions and electrons. For example, the application of a direct current (DC) bias or radio frequency (RF) bias can be used to accelerate the ions and retard the electrons from the plasma to the surface [3–5]. The sheath acts as an energy filter for the electrons, since only the very energetic electrons in the distribution can escape from the plasma to the

* Corresponding author. Fax: +886-7-5834861.
*E-mail addresses:* fbyeh@mail.cna.edu.tw (F.B. Yeh), pswei@mail.nsysu.edu.tw (P.S. Wei).
[1] Fax: +886-7-5254214/5254299.

0017-9310/$ - see front matter © 2004 Elsevier Ltd. All rights reserved.
doi:10.1016/j.ijheatmasstransfer.2004.06.004

## Nomenclature

| | |
|---|---|
| $c$ | particle thermal speed, $c^* = c/(K_B T_{e0}/m_i)^{1/2}$ |
| $D$ | Dawson function |
| $e$ | electron charge |
| $f$ | ion distribution function |
| $j$ | current density, $j^* = j/en_{e0}(K_B T_{e0}/m_i)^{1/2}$ |
| $k_B$ | Boltzmann constant |
| $m$ | particle mass |
| $M$ | ion-to-electron mass ratio, $M = m_i/m_e$ |
| $n$ | particle density, $n^* = n/n_{e0}$ |
| $p$ | mean pressure, $p^* = p/n_{eo}k_B T_{e0}$ |
| $q$ | fluid-like conduction heat, $q^* = q/[n_{eo}k_B T_{e0}(k_B T_{e0}/m_i)^{1/2}]$ |
| $Q$ | total energy flux, $Q^* = Q/[n_{eo}k_B T_{e0}(k_B T_{e0}/m_i)^{1/2}]$ |
| $T$ | temperature |
| $u$ | fluid velocity, $u^* = u/(k_B T_{e0}/m_i)^{1/2}$ |
| $U$ | ionization energy, $U_i^* = U_i/k_B T_{e0}$ |
| $x, y, z$ | Cartesian coordinate |
| $Z_i$ | ion charge number |

*Greek symbols*

| | |
|---|---|
| $\gamma$ | energy transmission factor, defined in Eq. (31) |
| $\varphi$ | work function, $\varphi^* = \varphi/k_B T_{e0}$ |
| $\kappa$ | electron-to-ion source temperature ratio at presheath edge $= T_{e0}/T_{i0}$ |
| $\rho$ | reflectivity |
| $\Xi$ | functions |
| $\tau$ | fluid-like viscous stress, $\tau^* = \tau/n_{eo}k_B T_{e0}$, |
| $\phi$, $\chi$ | dimensional and dimensionless potential, $\chi = -e\phi/k_B T_{e0}$ |
| $\Omega$ | function, defined in Eq. (6) |

*Superscript*

| | |
|---|---|
| * | dimensionless quantity |

*Subscripts*

| | |
|---|---|
| ab | absorption |
| b | boundary between sheath and presheath |
| e,i | electron and ion |
| rec | recombination |
| tot | total |
| w | wall |
| 0 | coordinate origin at $\phi = 0$ as shown in Fig. 1 |

surface. Thus the electron energy flux to the wall is lower than that which would occur if no sheath were present. The ions accelerated by the sheath voltage drop strike the surface with greater energy than would occur in the absence of a sheath. Investigation of the sheath and net current effects on the plasma, ion and electron energy fluxes therefore are of great scientific and technological importance.

The substrate bias effects on the plasma potential, deposition processes, and properties of deposition films in an electron cyclotron resonance plasma deposition have been studied by Shirai and Gonda [3]. They used a bias current–voltage analysis to measure plasma potential, and a Langmuir probe method to measure the floating potential on insulating and conducting substrates. The results showed that the plasma potential is independent of negative biases but sufficiently influenced by the positive biases. Increasing negative bias of the substrate enhanced deposition rates on the conducting substrate. The ion energy incident on the conducting substrate was not effectively changed for a positive bias. Thièry et al. [5] also experimentally investigated the effects of the substrate bias voltage on the properties of Cu film deposited by sputtering. The kinetic energy of argon ions coming from the plasma and impinging on the surface of growing films depends on the substrate bias voltage. The negative bias voltage thus can be changed to investigate the evolution of the deposition rate, surface roughness, microstructure, magnitude of residual stresses, and electrical resistivity of the film. It showed that the major characteristics of the copper film vary significantly with substrate bias voltage.

There has been intensive theoretical research to study energy and mass transport in the cathode or near wall region of electric arc discharges, lamps, fusion devices, edge plasmas, ion implantation, deposition, etching, etc. [6–11]. Predicting the total energy flux or the energy transmission factor [6], however, has been based on an incomplete and approximate intuition to include different components of energy fluxes. The particle and energy flows to an electrically biased probe immersed in magnetic field of the boundary plasma of a tokamak have been studied by Stangeby [12]. Kersten et al. [13] provided a general survey for energy balances on substrate surfaces during plasma processing. The mechanisms were focused on surface processes including heat radiation, kinetic and potential energies of charged particles and neutrals, and enthalpy of chemical surface reactions. A self-consistent and exact determination of the total energy from a kinetic analysis therefore is required. Rather complete kinetic analyses have been provided by Emmert et al. [14] and Wei et al. [15,16]. The former treated the wall completely absorbing the electrons and ions, while the latter allowed the wall

partially reflecting or secondly emitting ions and electrons.

This study is to analytically and systematically determine energy transport to a biased surface, which partially reflects or secondly emits ions and electrons. The ions and electrons are of highly non-Maxwell–Boltzmann velocity distributions [15,16]. Reflections of ions and electrons are commonly encountered in sputter etching and deposition, ion implantation, and an analytical technique known as ion scattering spectroscopy [17]. Plasma energy flux is composed of ion and electron energies and recombination energy at the surface. Accounting for the externally biased voltage, the total ion and electron energies and their components at the wall and sheath edge are determined. Manifestations of the sheath behavior and net current density affecting the plasma, ion and electron energy fluxes are also presented.

## 2. Kinetic model and analysis

In this work, a plasma composed of a presheath and sheath is in contact with a wall partially reflecting and secondly emitting ions and electrons, as illustrated in Fig. 1. In view of negative wall potential relative to the bulk plasma, the ions are accelerated and the electrons are retarded in the positive $x$-direction toward the wall. The ions and electrons without sufficient energy to overcome potential barrier experience turning in the negative and positive directions, respectively. The major assumptions made are as follows [16]:

1. This is a quasi-steady, one-dimensional model to predict energy transport in a thin thickness of the region considered. Velocity distributions of the ions and electrons are self-consistently determined from kinetic Boltzmann equation, those moving in the transverse directions are of Maxwell–Boltzmann distributions. The one-dimensional ion flow is suitable for the presheath and sheath imposed by a magnetic field which is negligibly small or in the direction parallel to the ion flow.
2. The transport processes in the plasma in contact with the surface can be modeled as those in the plasma between two parallel plates.
3. The workpiece surface is electrically negative biased.
4. The presheath and sheath are collisionless. The collisionless presheath is generally applicable for weakly ionized plasmas of low temperature inert gases. In discharge and manufacturing processing, temperature of the plasma near the wall is usually less than 1 eV (namely, 11,605 K) [8]. Aside from low densities of charged particles, electron impact excitation and ionization for inelastic collisions in an inert gas can be ignored for electron energy less than 5 eV [18]. The charge exchange collisions become insignificant for high ionization energy of the inert gas [18]. Since ionization is required to supply ion loss to the wall, determination of ionization rate in the presheath is still needed and referred to the often-used Emmert et al.'s model [14]. This model without accounting for kinetic mechanisms of collisions is based on the fact that the ions would be a Maxwell–Boltzmann distribution in the absence of an electrostatic field far from the wall. This proposition has been confirmed by measurements of the ion distribution functions from Bachet et al. [19], and successful comparisons between the measured ion density and velocity in argon plasma from Goeckner et al. [20] and this work, as can be seen later. Since inert gases and low densities of charged particles are considered, chemical reactions and the existence of negative ions can be neglected. Radiation due to free–free, free–bound, bound–bound collisions are also ignored [21]. Dissociations and rotational and vibrational excitations, etc. are absent if molecular collisions are excluded.
5. The effects of neutral particles are ignored.
6. Ion and electron reflectivities are constant. The effects of secondary emissions of the ions and electrons can be included into the reflectivities [22]. Thermionic and field emissions of the ions and electrons are ignored.

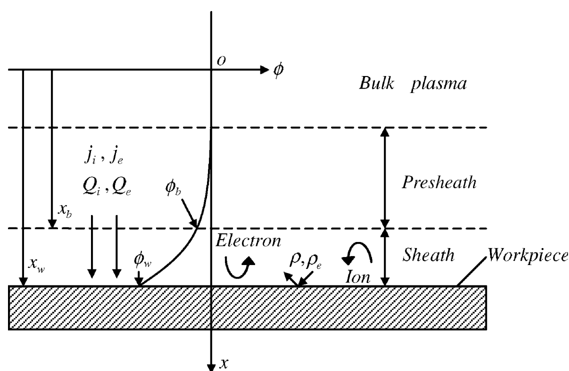


Fig. 1. System sketch for the model and coordinates.

### 2.1. Transport variables and potentials for a biased surface

Dimensionless ion density, fluid velocity, mean pressure, and fluid-like viscous stress and conduction heat at the sheath edge derived from different moments of the ion distribution function are, respectively, [16]

$$n_{ib}^* = \frac{1}{Z_i} e^{-\chi_b} \quad (1)$$

$$u_{ib}^* = \Omega_{1b} \tag{2}$$

$$p_{ib}^* = \frac{n_{ib}^*}{3\kappa}(\Omega_{2b} - \kappa u_{ib}^{*^2} + 2) \tag{3}$$

$$\tau_{ib}^* = 2\left(\frac{n_{ib}^*}{\kappa} - p_{ib}^*\right) \tag{4}$$

$$q_{ib}^* = -\tfrac{1}{2}n_{ib}^* u_{ib}^{*^3} - \tfrac{5}{2}u_{ib}^* p_{ib}^* + u_{ib}^*\tau_{ib}^* + Z_i n_{ib}^* u_{ib}^*\Omega \tag{5}$$

where function

$$\Omega \equiv \left[\frac{2}{Z_i\kappa} - 1 + \frac{\sqrt{\chi_b}}{D(\sqrt{\chi_b})}\right] \tag{6}$$

Dawson function $D(\sqrt{x})$ and functions $\Omega_{1b}$, $\Omega_{2b}$ in Eqs. (6), (2) and (3) are defined in [16]. The dimensionless sheath edge potential in Eqs. (1) and (6) is satisfied by

$$\frac{2}{\sqrt{\pi Z_i\kappa}}D(\sqrt{\chi_b}) = e^{Z_i\kappa\chi_b}\mathrm{erfc}(\sqrt{Z_i\kappa\chi_b}) \tag{7}$$

where $\mathrm{erfc}(\sqrt{x})$ is the complementary error function. The corresponding dimensionless transport variables of the ions and electrons in the sheath are, respectively [16]

$$n_i^* = \frac{1}{Z_i}\{\Xi_2(\chi) + e^{Z_i\kappa\chi}\mathrm{erfc}[\sqrt{Z_i\kappa(\chi-\chi_b)}] - \Xi_1(\chi)\} \tag{8}$$

$$u_i^* = \frac{1}{n_i^* Z_i}e^{-\chi_b}\Omega_{1b} \tag{9}$$

$$p_i^* = \frac{1}{3}\left[\Xi_3(\chi) - n_i^* u_i^{*^2} + \frac{2}{\kappa}n_i^*\right] \tag{10}$$

$$\tau_i^* = n_i^* u_i^{*^2} + p_i^* - Z_i E_i^* - n_{ib}^* u_{ib}^{*^2} - p_{ib}^* + \tau_{ib}^* \tag{11}$$

$$\begin{aligned} q_i^* = {} & -\tfrac{1}{2}n_i^* u_i^{*^3} - \tfrac{5}{2}u_i^* p_i^* + u_i^*\tau_i^* + Z_i u_i^* n_i^*\chi + q_{ib}^* \\ & + \tfrac{1}{2}n_{ib}^* u_{ib}^{*^3} + \tfrac{5}{2}u_{ib}^* p_{ib}^* - u_{ib}^*\tau_{ib}^* - Z_i u_{ib}^* n_{ib}^*\chi_b \end{aligned} \tag{12}$$

$$n_e^* = e^{-\chi}\left[1 + \frac{\rho_e - 1}{2}\mathrm{erfc}(\sqrt{\chi_w - \chi})\right] \tag{13}$$

$$u_e^* = \frac{(1-\rho_e)}{n_e^*}\sqrt{\frac{M}{2\pi}}e^{-\chi_w} \tag{14}$$

$$p_e^* = \frac{1}{3}\left[\Xi_4(\chi) - \frac{1}{M}n_e^* u_e^{*^2} + 2n_e^*\right] \tag{15}$$

$$\tau_e^* = 2(n_e^* - p_e^*) \tag{16}$$

$$q_e^* = n_e^* u_e^*(\chi_w - \chi + 1) - \frac{3}{2}u_e^*\Xi_4(\chi) + \frac{1}{M}n_e^* u_e^{*^3} \tag{17}$$

where dimensionless functions $\Xi_1(\chi)$, $\Xi_2(\chi)$, $\Xi_3(\chi)$, $\Xi_4(\chi)$ and electrical field intensity $E_i^*$ are defined in [16]. The dimensionless net current density at the wall is given by

$$j^* = j_{iw}^* - j_{ew}^* \tag{18}$$

where the ion and electron current densities at the wall are, respectively,

$$j_{iw}^* = Z_i n_{iw}^* u_{iw}^* = Z_i n_{ib}^* u_{ib}^*, \qquad j_{ew}^* = n_{ew}^* u_{ew}^* = n_{eb}^* u_{eb}^* \tag{19}$$

Eq. (18) is the coupling relationship between the electrons and ions. The dimensionless wall potential is determined by substituting Eqs. (19), (8), (9), (13) and (14) into Eq. (18)

$$\chi_w = \ln\left(\frac{1-\rho_e}{j_{iw}^* - j^*}\sqrt{\frac{M}{2\pi}}\right) \tag{20}$$

When net current density $j^* = 0$, the wall is electrically floating, while the externally biased effect is strong for $j^* \to j_{iw}^*$.

### 2.2. Plasma energy transport to a biased surface

The dimensional total energy flux of the ions at a location is given by [23]

$$Q_i = \int_{-\infty}^{\infty} f_i \frac{1}{2}m_i(c_x^2 + c_y^2 + c_z^2)c_x\,dc_x\,dc_y\,dc_z \tag{21}$$

where $f_i$ is the ion distribution function. Integrating Eq. (21) by introducing the ion distribution function [16], dimensionless ion energy flux in the sheath leads to

$$Q_i^* = \tfrac{1}{2}n_i^* u_i^{*^3} + \tfrac{5}{2}u_i^* p_i^* - u_i^*\tau_i^* + q_i^* \tag{22}$$

where the terms on the right-hand side represent ion kinetic energy, flow work, energy fluxes due to fluid-like viscous stress and conduction heat, respectively. Substituting Eq. (5), Eq. (22) gives dimensionless ion energy flux at the sheath edge

$$Q_{ib}^* = \tfrac{1}{2}n_{ib}^* u_{ib}^{*^3} + \tfrac{5}{2}u_{ib}^* p_{ib}^* - u_{ib}^*\tau_{ib}^* + q_{ib}^* = j_{ib}^*\Omega \tag{23}$$

Combining Eqs. (12) and (22), the dimensionless ion energy flux at the wall is found to be

$$\begin{aligned} Q_{iw}^* &= \tfrac{1}{2}n_{iw}^* u_{iw}^{*^3} + \tfrac{5}{2}u_{iw}^* p_{iw}^* - u_{iw}^*\tau_{iw}^* + q_{iw}^* \\ &= Q_{ib}^* + j_{iw}^*(\chi_w - \chi_b) = j_{iw}^*[\Omega + (\chi_w - \chi_b)] \end{aligned} \tag{24}$$

The dimensional total energy flux of the electrons at a location is given by [23]

$$Q_e = \int_{-\infty}^{\infty} f_e \frac{1}{2}m_e(c_x^2 + c_y^2 + c_z^2)c_x\,dc_x\,dc_y\,dc_z \tag{25}$$

where $f_e$ is the electron distribution function. Substituting the electron distribution function [16] and integrating Eq. (25), dimensionless electron energy flux in the sheath is found to be

$$Q_e^* = \frac{1}{2M}n_e^* u_e^{*^3} + \frac{5}{2}u_e^* p_e^* - u_e^*\tau_e^* + q_e^* \tag{26}$$

Substituting Eqs. (13)–(17) into Eq. (26), the dimensionless electron energy flux at the sheath edge is given by

$$Q^*_{\rm eb} = \frac{1}{2M} n^*_{\rm eb} u^{*^3}_{\rm eb} + \frac{5}{2} u^*_{\rm eb} p^*_{\rm eb} - u^*_{\rm eb} \tau^*_{\rm eb} + q^*_{\rm eb}$$
$$= j^*_{\rm eb}[2 + (\chi_{\rm w} - \chi_{\rm b})] \quad (27)$$

The dimensionless electron energy flux at the wall is

$$Q^*_{\rm ew} = Q^*_{\rm eb} - j^*_{\rm ew}(\chi_{\rm w} - \chi_{\rm b}) = 2j^*_{\rm ew}$$
$$= (1 - \rho_{\rm e})\sqrt{\frac{2M}{\pi}} {\rm e}^{-\chi_{\rm w}} \quad (28)$$

As an ion hits the surface, it recombines with electrons and deposits energy equal to the difference between the ionization energy $U_{\rm i}$ and work function $Z_{\rm i}\varphi$ to the wall. The dimensionless total energy flux transferred to the biased surface then yields

$$Q^*_{\rm totw} = Q^*_{\rm iw} + Q^*_{\rm ew} + Q^*_{\rm rec} + Q^*_{\rm ab}$$
$$= j^*_{\rm iw}\left(\Omega + \chi_{\rm w} - \chi_{\rm b} + \frac{U^*_{\rm i}}{Z_{\rm i}} - \varphi^*\right) + j^*_{\rm ew}(2 + \varphi^*) \quad (29)$$

where dimensionless energies for recombination and absorption of an electron coming from the plasma are, respectively, [7]

$$Q^*_{\rm rec} = j^*_{\rm iw}\left(\frac{U^*_{\rm i}}{Z_{\rm i}} - \varphi^*\right), \qquad Q^*_{\rm ab} = j^*_{\rm ew}\varphi^* \quad (30)$$

Eq. (29) shows that the total energy flux transport to the wall depends on ion and electron fluxes, the difference in potentials between the surface and sheath edge, and recombination energies of the ions and electrons. The total dimensionless energy flux at the wall for a floating wall can be calculated from Eq. (29) by setting $j^*_{\rm iw} = j^*_{\rm ew}$. The error and Dawson functions were numerically integrated by a Simpson's rule. Errors were less than $10^{-6}$ by comparing grids of 1000 and 500.

## 3. Results and discussion

In this study, independent parameters controlling plasma energy transport processes in a presheath and sheath are ion reflectivity ($\rho$) and electron reflectivity ($\rho_{\rm e}$) of the wall, ion-to-electron mass ratio ($M$), charge number ($Z_{\rm i}$), electron-to-ion source temperature ratio at the presheath edge ($\kappa$), net current density ($j^*$), recombination energy ($U^*_{\rm i}$), and work function ($\varphi^*$).

To confirm relevancy and accuracy of this model, the predicted energy transmission factor between a helium plasma and tungsten workpiece as a function of dimensionless wall potential is compared with experimental data provided by Masuzaki et al. [24], as shown in Fig. 2. The energy transmission factor $\gamma$ is defined as [6]

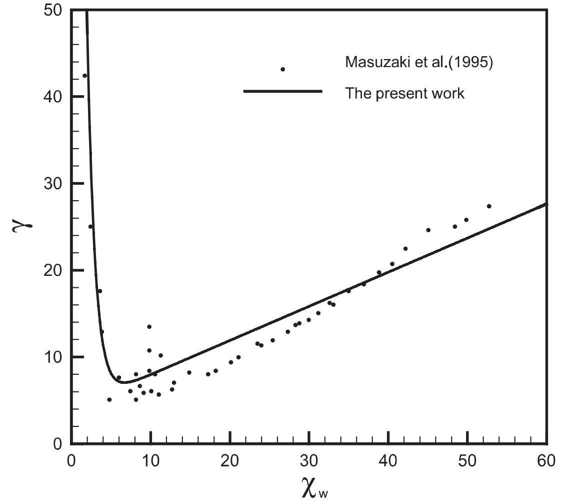


Fig. 2. A comparison between the predicted energy transmission factor as a function of dimensionless wall potential and experimental result [24].

$$\gamma = \frac{Q_{\rm totw}}{k_{\rm B}T_{\rm e}n_{\rm ib}(k_{\rm B}T_{\rm e}/m_{\rm i} + k_{\rm B}T_{\rm i}/m_{\rm i})^{1/2}}$$
$$= \frac{Q^*_{\rm totw}}{n^*_{\rm ib}}\left(1 + \frac{1}{\kappa}\right)^{-1/2} \quad (31)$$

where the electron temperature at the sheath edge is considered to be identical to that at the presheath edge, while the ion temperature at the sheath edge is the ion source temperature at the presheath edge. Choosing dimensionless parameters $Z_{\rm i} = 1$, $\rho = 0.47$, $\rho_{\rm e} = 0$, $M = 7344$, $\kappa = 10$, $U^*_{\rm i} = 14.3$, $\varphi^* = 2.5$, the predicted energy transmission factor as a function of wall potential agrees well with experimental data [24]. Deviation can be due to the unavailable ion and electron temperatures at the sheath edge. Good comparisons between the predicted and measured ion density and velocity as a function of potential [20] for an argon plasma and stainless steel workpiece are also shown in Fig. 3. The data chosen for comparison are $Z_{\rm i} = 4$, $\rho = \rho_{\rm e} = 0$, $M = 72{,}817$, $\kappa = 0.02$, and $n_{\rm e0} = 2.3 \times 10^{14}$ m$^{-3}$, $m_{\rm i} = 6.68 \times 10^{-26}$ kg, $T_{\rm e0} = 1.874 \times 10^3$ K, $\phi_{\rm w} = -100$ V.

Spatial variations of dimensionless ion energy flux and its components, including fluid kinetic energy, energies due to mean pressure (namely, the flow work), fluid-like viscous stress and conduction heat, in the sheath for different ion reflectivities and dimensionless net current densities are shown in Fig. 4. Since electrostatic potential is a function of spatial position, the abscissa representing dimensionless electrostatic potential also indicates spatial locations in the sheath [16]. Dimensionless potential of 0.404 is referred to the sheath edge, while dimensionless potential of 2.965, 3.804,

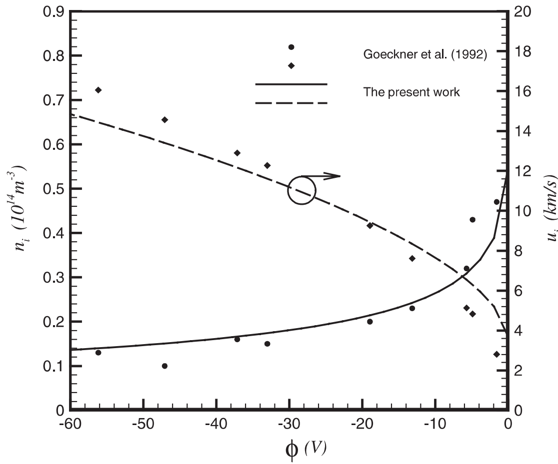


Fig. 3. A comparison between the theoretical predicted ion density and velocity as a function of potential and experimental results [20].

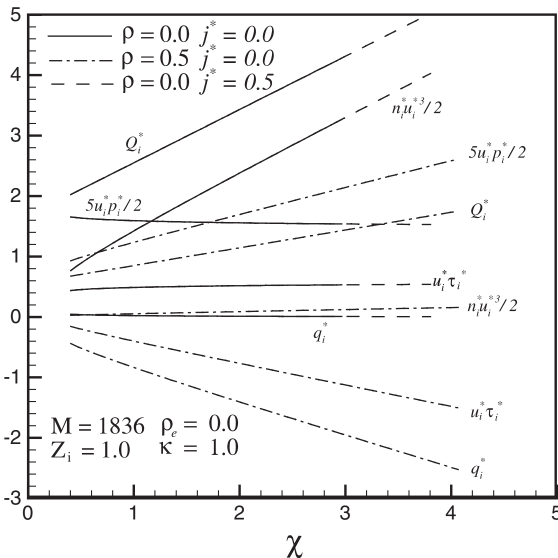


Fig. 4. Spatial variations of dimensionless total ion energy ($Q_i^*$), fluid kinetic energy ($n_i^* u_i^{*3}/2$), flow work ($5n_i^* p_i^*/2$), and fluid-like viscous stress energy ($u_i^* \tau_i^*$) and conduction heat ($q_i^*$) in sheath for different ion reflectivities ($\rho$) and net current densities ($j^*$).

and 4.064 are the wall for $\rho = 0$, $j^* = 0$, $\rho = 0$, $j^* = 0.5$, and $\rho = 0.5$, $j^* = 0$, respectively. It can be seen that increases of net current density and ion reflectivity enhance dimensionless wall potential to reduce electron and ion currents, respectively. The variations of dimensionless ion energy flux, fluid kinetic energy, flow work, and energies due to fluid-like viscous stress and conduction heat with dimensionless potential are independent of net current density (see Eqs. (1)–(12)). In view of an increase in fluid speed [16], fluid kinetic energy increases with decreasing ion reflectivity. In contrast to zero ion reflectivity, dimensionless flow work increases in the forward direction for ion reflectivity of 0.5. This is attributed to retardation of ion flow by increasing mean pressure [16]. Fluid-like conduction heat energy flux is directed from the sheath edge to the wall for zero ion reflectivity, in contrast to that for ion reflectivity of 0.5. Since fluid-like viscous stress acts as a driving force for zero ion reflectivity and a retarding force for ion reflectivity of 0.5 [16], the corresponding energy fluxes are positive and negative, respectively. Due to the dominant fluid kinetic energy, ion energy flux is increased by decreasing ion reflectivity. Irrespective of ion reflectivity and net current, dimensionless ion energy flux and fluid kinetic energy increase monotonically in the forward direction.

Similar dimensionless quantities of the electrons across the sheath for different ion reflectivities and dimensionless net current densities are presented in Fig. 5. It is found that dimensionless electron energy flux, flow work and fluid-like conduction heat decrease, and fluid kinetic energy and energy due to fluid-like viscous stress increase in the forward direction. In contrast to the ions, fluid-like viscous stress of the electrons is a driving force and conduction heat directs toward the wall for different net currents and ion reflectivities. Due to reduction of electron current from an enhanced wall potential, electron energy flux and its components decrease with increasing net current and ion reflectivity.

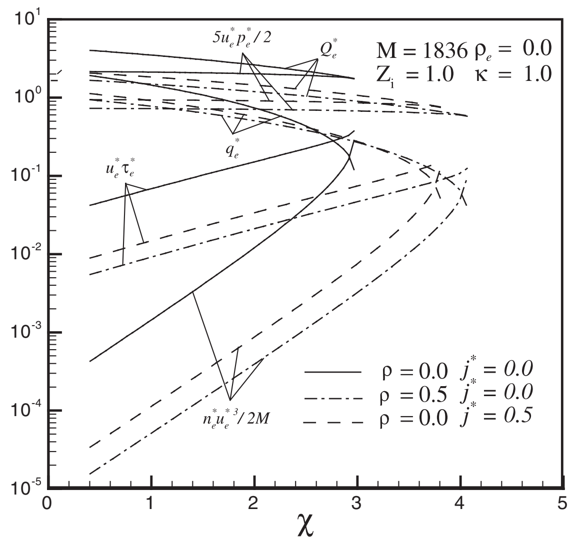


Fig. 5. Spatial variations of dimensionless total electron energy ($Q_e^*$), fluid kinetic energy ($n_e^* u_e^{*3}/2M$), flow work ($5n_e^* p_e^*/2$), and fluid-like viscous stress energy ($u_e^* \tau_e^*$) and conduction heat ($q_e^*$) in sheath for different ion reflectivities ($\rho$) and net current densities ($j^*$).

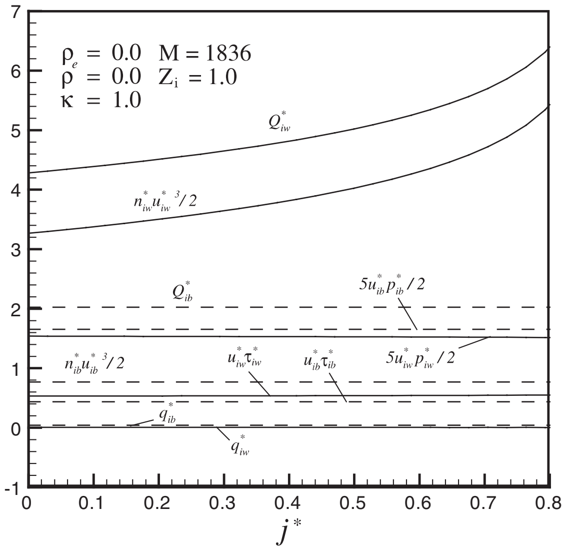


Fig. 6. Dimensionless total ion energies ($Q^*_{ib}, Q^*_{iw}$), fluid kinetic energies ($n^*_{ib}u^{*3}_{ib}/2, n^*_{iw}u^{*3}_{iw}/2$), flow works ($5n^*_{ib}p^*_{ib}/2, 5n^*_{iw}p^*_{iw}/2$), and fluid-like viscous stress energies ($u^*_{ib}\tau^*_{ib}, u^*_{iw}\tau^*_{iw}$) and conduction heats ($q^*_{ib}, q^*_{iw}$) at sheath edge and wall versus net current density ($j^*$).

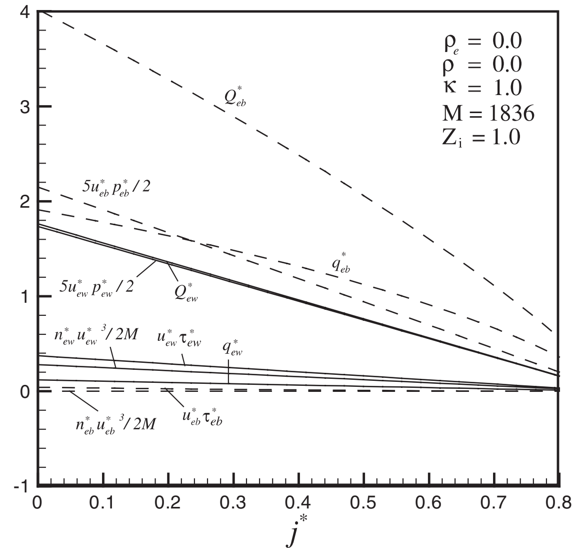


Fig. 7. Dimensionless total electron energies ($Q^*_{eb}, Q^*_{ew}$), fluid kinetic energies ($n^*_{eb}u^{*3}_{eb}/2M, n^*_{ew}u^{*3}_{ew}/2M$), flow works ($5n^*_{eb}p^*_{eb}/2, 5n^*_{ew}p^*_{ew}/2$), and fluid-like viscous stress energies ($u^*_{eb}\tau^*_{eb}, u^*_{ew}\tau^*_{ew}$) and conduction heats ($q^*_{eb}, q^*_{ew}$) at sheath edge and wall versus net current density ($j^*$).

The effects of dimensionless net current on ion energy flux and its components at the sheath edge and wall are shown in Fig. 6. In contrast to flow work and fluid-like conduction heat, dimensionless ion energy flux, fluid kinetic energy, and energy due to fluid-like viscous stress at the wall are higher than those at the sheath edge. Even though energies at the sheath edge remain constant, dimensionless ion energy flux, fluid kinetic energy, energy due to fluid-like viscous stress at the wall increase, and flow work, fluid-like conduction heat decrease slightly with increasing net current. For dimensionless net current densities of 0 and 0.8, the corresponding dimensionless ion energy fluxes at the wall are around 4.28 and 6.4, respectively, and dimensionless ion energy flux at the sheath edge is 2.03. The ratios of ion energy fluxes between the wall and sheath edge therefore are 2.1 and 3.2, respectively. In the absence of the sheath, ion energy flux is seriously underestimated for a high net current density.

Similar dimensionless quantities of the electrons versus net current density are presented in Fig. 7. Owing to reduction of electron current, dimensionless electron energy flux and its components decrease with increasing net current density. Rather than fluid kinetic energy and energy due to fluid-like viscous stress, dimensionless electron energy flux, flow work, and fluid-like conduction heat at the wall are lower than those at the sheath edge. This is attributed to negative work exerted by electrostatic field on the electrons in the sheath. For net currents of 0 and 0.8, the corresponding dimensionless electron energy fluxes at the wall are around 1.76 and 0.18, while those at the sheath edge are 4.02 and 0.6, respectively. The ratios of electron energy fluxes at the sheath edge and wall therefore are 2.28 and 3.33, respectively. Without the sheath, electron energy flux is seriously overestimated for a high net current density.

The variations in dimensionless potentials, current densities of ions and electrons, electrical potential energy, ion and electron energy fluxes and total energy fluxes at a floating wall and sheath edge with ion reflectivity are shown in Fig. 8. The total energy flux is the sum of the total ion and electron energy fluxes. An increase of ion reflectivity increases dimensionless wall potential while sheath edge potential maintains constant [16]. In view of a decrease in ion speed at the sheath edge, dimensionless electron and ion current densities, electrical potential energy, ion and electron energy fluxes at the sheath edge and wall decrease with increasing ion reflectivity. Dimensionless energy flux of the electrons is less than that of the ions at the wall in contrast to those at the sheath edge. Since the ions gain energy from work done by electrostatic field while the electrons lose the same energy in the forward direction toward the floating wall, dimensionless ion energy flux at the wall is greater than that at the sheath in contrast to electron energy flux. The total energy fluxes of the ions and electrons at the sheath edge and wall also maintain the same. It is found that the ion-to-electron energy flux ratio at the wall increases with ion reflectivity. As ion reflectivity increases, contribution of electrical potential energy to

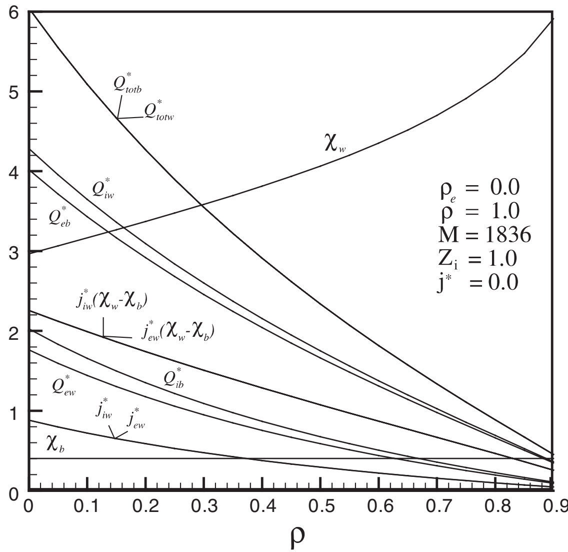


Fig. 8. Dimensionless sheath edge and wall potentials ($\chi_b, \chi_w$), ion and electron energy fluxes ($Q^*_{ib}, Q^*_{eb}, Q^*_{iw}, Q^*_{ew}$) and total energy fluxes ($Q^*_{totb}, Q^*_{totw}$) at sheath edge and wall, ion and electron current densities ($j^*_{iw}, j^*_{ew}$) and potential energies ($j^*_{iw}(\chi_w - \chi_b), j^*_{ew}(\chi_w - \chi_b)$) at wall versus ion reflectivity ($\rho$).

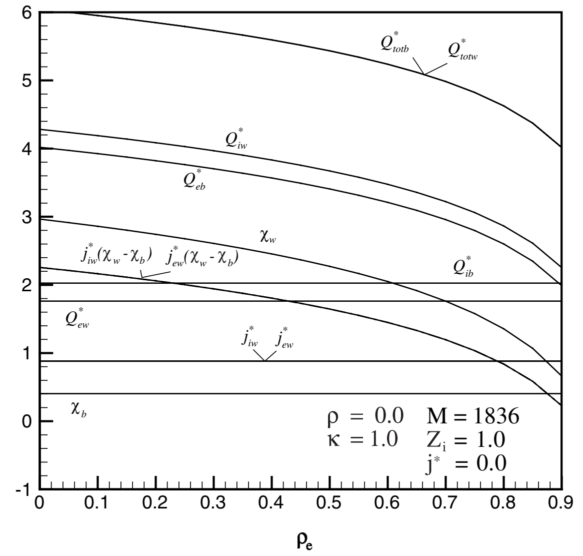


Fig. 9. Dimensionless sheath edge and wall potentials ($\chi_b, \chi_w$), ion and electron energy fluxes ($Q^*_{ib}, Q^*_{eb}, Q^*_{iw}, Q^*_{ew}$) and total energy fluxes ($Q^*_{totb}, Q^*_{totw}$) at sheath edge and wall, ion and electron current densities ($j^*_{iw}, j^*_{ew}$) and potential energies ($j^*_{iw}(\chi_w - \chi_b), j^*_{ew}(\chi_w - \chi_b)$) at wall versus electron reflectivity ($\rho_e$).

the total energy flux at the wall is greater than that at the sheath edge.

The effects of electron reflectivity on dimensionless total ion and electron energy fluxes and their components subject to a floating wall are presented in Fig. 9. Dimensionless wall potential decreases with increasing electron reflectivity, while sheath edge potential remains constant [16]. Dimensionless sheath edge potential, ion and electron current densities and electron energy flux at the wall, and ion energy flux at the sheath edge are independent of electron reflectivity. In view of a decrease in dimensionless wall potential, electrical potential energy decreases with increasing electron reflectivity. Dimensionless ion energy flux at the wall and electron energy flux at the sheath edge thus decrease with increasing electron reflectivity. Since dimensionless ion and electron energy fluxes at the sheath edge approach those at the wall, the effects of sheath on ion and electron energy fluxes can be neglected for a high electron reflectivity. The ion-to-electron energy flux ratio and total energy flux at the wall decrease with increasing electron reflectivity.

The effects of electron-to-ion source temperature ratio at the presheath edge on dimensionless ion and electron energy fluxes and their components at the sheath edge and wall are shown in Fig. 10. It is seen that dimensionless sheath edge and wall potentials increase with increase electron-to-ion source temperature ratio [16]. This is attributed to that ion generation rate is low

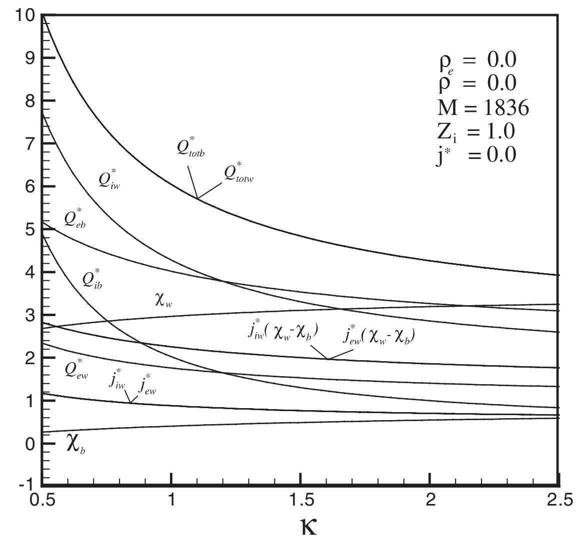


Fig. 10. Dimensionless sheath edge and wall potentials ($\chi_b, \chi_w$), ion and electron energy fluxes ($Q^*_{ib}, Q^*_{eb}, Q^*_{iw}, Q^*_{ew}$) and total energy fluxes ($Q^*_{totb}, Q^*_{totw}$) at sheath edge and wall, ion and electron current densities ($j^*_{iw}, j^*_{ew}$) and potential energies ($j^*_{iw}(\chi_w - \chi_b), j^*_{ew}(\chi_w - \chi_b)$) at wall versus electron–ion source temperature ratio at presheath edge ($\kappa$).

for a high electron-to-ion source temperature ratio. Dimensionless electron and ion current densities and

different energy fluxes decrease with increasing electron-to-ion source temperature ratio. Although dimensionless wall potential increases with electron-to-ion source temperature ratio, decreases of ion and electron current densities reduce electrical potential energy at the wall. The ion-to-electron energy flux ratio at the wall decreases with increasing electron-to-ion source temperature ratio.

Dimensionless current densities and energy fluxes of the ions and electrons, and sheath edge and wall potentials versus the ion-to-electron mass ratio are shown in Fig. 11. Dimensionless sheath edge potential, ion and electron current densities, ion energy flux at the sheath edge, and electron energy flux at the wall are independent of ion-to-electron mass ratio. Increasing ion-to-electron mass ratio enhances dimensionless wall potential, which increases dimensionless electrical potential energy, ion energy flux and total energy flux at the wall. The constant dimensionless electron energy flux at the wall is due to the constant dimensionless electron current density (see Eq. (28)). The effects of charge number on dimensionless current densities and energy fluxes of the ions and electrons, and sheath edge and wall potentials are presented in Fig. 12. In contrast to wall potential and ion energy fluxes at the wall and sheath edge, dimensionless sheath edge potential, ion and electron current densities, electron energy fluxes at the wall and the sheath edge increase with charge number. The dimensionless total energy flux and electrical potential energy decrease and then slightly increase with increasing charge number. The minimum of the former taking place at a charge number of 2 is a result of an increase in dimensionless electron energy flux at the wall and decrease of ion energy flux with increasing charge number. The minimum of the latter taking place at a charge number of around 1.1 is due to an increase in current density and a decrease in dimensionless potential drop with increasing charge number.

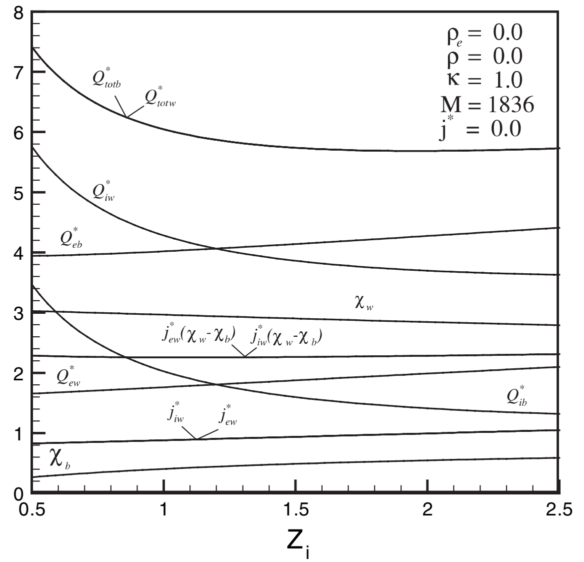


Fig. 12. Dimensionless sheath edge and wall potentials $(\chi_b, \chi_w)$, ion and electron energy fluxes $(Q^*_{ib}, Q^*_{eb}, Q^*_{iw}, Q^*_{ew})$ and total energy fluxes $(Q^*_{totb}, Q^*_{totw})$ at sheath edge and wall, ion and electron current densities $(j^*_{iw}, j^*_{ew})$ and potential energies $(j^*_{iw}(\chi_w-\chi_b), j^*_{ew}(\chi_w-\chi_b))$ at wall versus charge number $(Z_i)$.

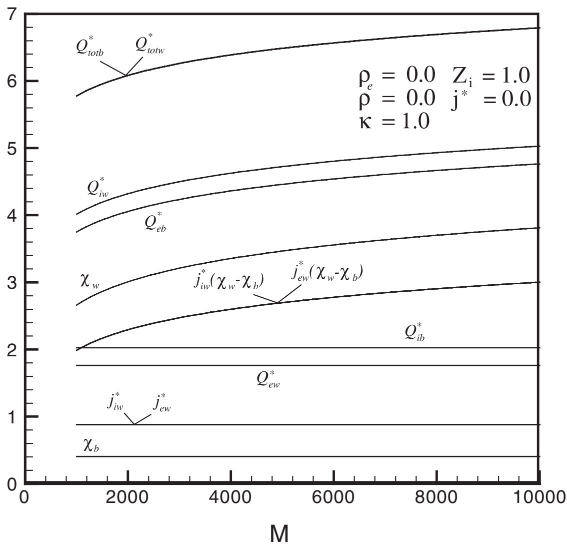


Fig. 11. Dimensionless sheath edge and wall potentials $(\chi_b, \chi_w)$, ion and electron energy fluxes $(Q^*_{ib}, Q^*_{eb}, Q^*_{iw}, Q^*_{ew})$ and total energy fluxes $(Q^*_{totb}, Q^*_{totw})$ at sheath edge and wall, ion and electron current densities $(j^*_{iw}, j^*_{ew})$ and potential energies $(j^*_{iw}(\chi_w-\chi_b), j^*_{ew}(\chi_w-\chi_b))$ at wall versus ion–electron mass ratio $(M)$.

Dimensionless current densities, energy fluxes of the ions and electrons at the wall and sheath edge, wall and sheath edge potentials versus net current density are presented in Fig. 13. An increase in net current reduces electron current density and enhances dimensionless potential at the wall. This is because potential and ion current density at the sheath edge are independent of net current. As discussed previously, in contrast to the electrons, dimensionless ion energy flux at the sheath edge is lower than that at the wall. Rather than that at the wall, energy flux of the electrons is higher than that of ions at the sheath edge for a low net current density. The ratio between ion and electron energy fluxes at the wall rapidly increases with net current. In view of an increase in potential drop, electrical potential energy and energy flux of the ions at the wall increase with net current. On the other hand, decreases in electrical potential energy and energy flux of the electrons at the wall with increasing net current density are resulted from a decrease in electron current density. The ratio between the ion energy flux (and electrical potential energy flux)

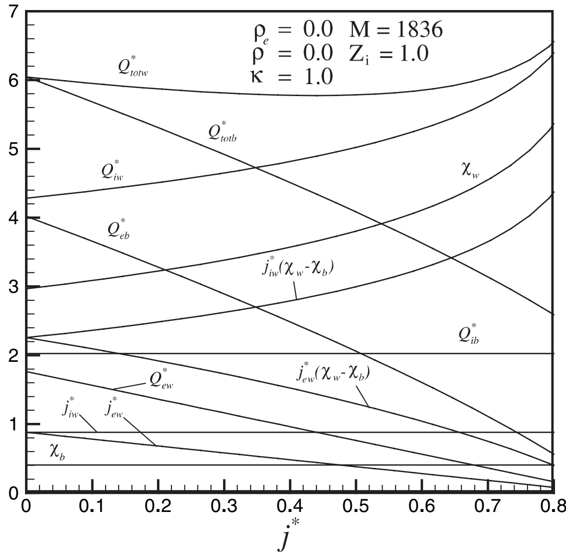


Fig. 13. Dimensionless sheath edge and wall potentials ($\chi_b, \chi_w$), ion and electron energy fluxes ($Q^*_{ib}, Q^*_{eb}, Q^*_{iw}, Q^*_{ew}$) and total energy fluxes ($Q^*_{totb}, Q^*_{totw}$) at sheath edge and wall, ion and electron current densities ($j^*_{iw}, j^*_{ew}$) and potential energies ($j^*_{iw}(\chi_w - \chi_b)$, $j^*_{ew}(\chi_w - \chi_b)$) at wall versus net current density ($j^*$).

and the total energy flux increases with net current. It is noted that the total energy flux at the wall has the minimum at dimensionless net current density of around 0.45. This is attributed to an increase in ion energy flux and a decrease in electron energy flux at the wall with increasing net current.

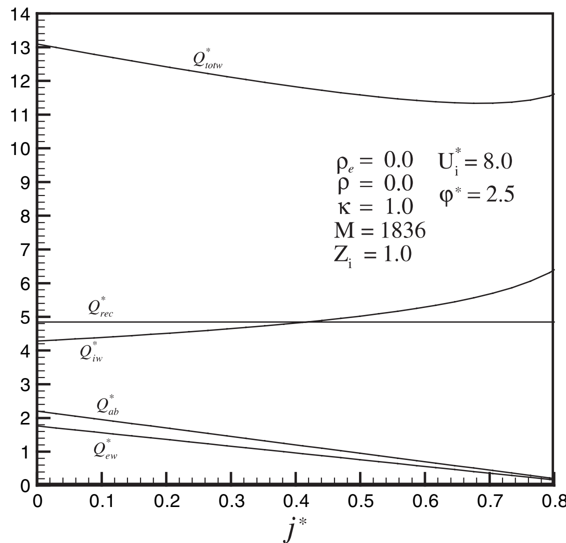


Fig. 14. Dimensionless total energy flux ($Q^*_{totw}$), ion and electron energy fluxes ($Q^*_{iw}, Q^*_{ew}$), recombination energy ($Q^*_{rec}$), and absorption energy ($Q^*_{ab}$) at wall versus net current density ($j^*$).

The effects of the dimensionless recombination and absorption energies on energy transfer to a wall are shown in Fig. 14. Dimensionless ionization energy of 8 and work function of 2.5 correspond to ionization energy of 13.6 eV for hydrogen plasma and work function of 4.55 eV for a tungsten workpiece, respectively. The constant dimensionless recombination energy of the ions is resulted from constant ion current density. In view of a decrease in electron current density, energy released from absorption of electrons at the wall decreases with increasing net current. It is noted that the recombination energy is greater than other components under floating and slightly biased conditions. Referring to Fig. 13 shows that accounting for recommendation and absorbed energies from ions and electrons increases the dimensionless total energy flux at the wall from 6.05 to 13.1 and 6.5 to 11.6 at dimensionless net current densities of 0 and 0.8, respectively.

## 4. Conclusions

The conclusions drawn are the following:

1. The predicted energy transmission factor, ion density and velocity as a function of potential based on the kinetic analysis agree well with experimental data.
2. The dimensionless total energy fluxes at the wall and sheath edge increase with decreasing ion and electron reflectivities, electron-to-ion source temperature ratio at the presheath edge, and increasing ion-to-electron mass ratio. However, as charge number increases, dimensionless total energy fluxes at the wall and sheath edge decrease and then slightly increase. Since an increase of net current enhances and reduces energy fluxes of the ions and electrons at the wall, respectively, the total energy flux at the wall exists a minimum value. The total energy flux at the sheath edge, however, decreases with increasing net current.
3. Dimensionless ion energy flux at the wall is increased by decreasing ion and electron reflectivities, electron-to-ion source temperature ratio, charge number, and increasing ion-to-electron mass ratio and net current. In contrast to that at the wall, ion energy flux at the sheath edge is increased by decreasing ion reflectivity, electron-to-ion source temperature ratio and charge number. Ion energy flux at the sheath edge, however, is independent of electron reflectivity, ion-to-electron mass ratio and net current.
4. Dimensionless electron energy flux at the sheath edge increases with decreasing ion and electron reflectivities, electron-to-ion source temperature ratio, net current, and increasing ion-to-electron mass ratio and charge number. Dimensionless electron energy flux at the wall rather than the sheath edge is increased by decreasing ion reflectivity, electron-to-ion source

temperature ratio, net current, and increasing charge number. Electron energy flux at the wall is independent of electron reflectivity and ion-to-electron mass ratio.

5. A decrease of ion-to-electron energy flux ratio at the wall is achieved by increasing electron reflectivity, electron-to-ion source temperature ratio, charge number and decreasing ion reflectivity, ion-to-electron mass ratio and net current.
6. The ratio of dimensionless ion energy flux at the wall to that at the sheath edge, and the ratio of electron energy flux at the sheath edge to that at the wall are increased by increasing ion reflectivity, electron-to-ion source temperature ratio, ion-to-electron mass ratio, net current, and decreasing electron reflectivity. Increasing charge number results in an increase of the former and a decrease of the latter. If the sheath is ignored, the ion and electron energy flux are, respectively, underestimated and overestimated.
7. The ratio of dimensionless total energy flux at the wall to that at the sheath edge are rapidly increased by increasing net current density. An account for the sheath to predict the total energy flux on a biased surface is crucial.

## References


[1] F.F. Chen, Introduction to Plasma Physics, Plenum Press, NY, 1974.

[2] D. Bohm, Minimum ionic kinetic energy for a stable sheath, in: A. Guthrie, R. Wakerling (Eds.), The Characteristics of Electrical Discharges in Magnetic Fields, McGraw-Hill, NY, 1949, pp. 77–86.

[3] K. Shirai, S. Gonda, Study of the substrate bias in plasma depositions using an electron cyclotron resonance plasma, J. Appl. Phys. 68 (1990) 4258–4267.

[4] M. Jin, K.C. Kao, The effects of substrate bias on microwave plasma etching, J. Vac. Sci. Technol. B 10 (1992) 601–610.

[5] F. Thièry, Y. Pauleau, L. Ortega, Effect of the substrate bias voltage on the physical characteristics of cooper films deposited by microwave plasma-assisted sputtering technique, J. Vac. Sci. Technol. A 22 (2004) 30–35.

[6] P.C. Stangeby, Plasma sheath transmission factors for tokamak edge plasmas, Phys. Fluids 27 (1984) 682–690.

[7] M.S. Benilov, A. Marotta, A model of the cathode region of atmospheric pressure arcs, J. Phys. D: Appl. Phys. 28 (1995) 1869–1882.

[8] K.C. Hsu, E. Pfender, Analysis of the cathode region of a free-burning high intensity argon arc, J. Appl. Phys. 54 (1983) 3818–3824.

[9] H. Schmitz, K.-U. Riemann, Analysis of the cathodic region of atmospheric pressure discharges, J. Phys. D: Appl. Phys. 35 (2002) 1727–1735.

[10] S. Takamura, M.Y. Ye, T. Kuwabara, N. Ohno, Heat flows through plasma sheaths, Phys. Plasmas 5 (1998) 2151–2158.

[11] D. Uhrlandt, D. Loffhagen, S. Arndt, R. Winkler, Current progress in the modeling of weakly ionized plasmas in contact with electrodes and insulated walls, Surf. Coat. Technol. 142–144 (2001) 517–525.

[12] P.C. Stangeby, Effect of bias on trapping probes and bolometers for tokamak edge diagnosis, J. Phys. D: Appl. Phys. 15 (1982) 1007–1029.

[13] H. Kersten, H. Deutsch, H. Steffen, G.M.W. Kroesen, R. Hippler, The energy balance at substrate surfaces during plasma processing, Vacuum 63 (2001) 385–431.

[14] G.A. Emmert, R.M. Wieland,, A.T. Mense, J.N. Davidson, Electric sheath and presheath in a collisionless, finite ion temperature plasma, Phys. Fluids 23 (1980) 803–812.

[15] P.S. Wei, F.B. Yeh, C.Y. Ho, Distribution function of positive ions and electrons in a plasma near a surface, IEEE Trans. Plasma Sci. 28 (2000) 1244–1253.

[16] P.S. Wei, F.B. Yeh, Fluid-like transport variables in a kinetic, collisionless plasma near a surface with ion and electron reflection, IEEE Trans. Plasma Sci. 28 (2000) 1233–1243.

[17] B. Chapman, Glow Discharge Processes, Sputtering and Plasma Etching, Wiley, NY, 1980.

[18] M.A. Lieberman, A.J. Lichtenberg, Principles of Plasma Discharges and Materials Processing, Wiley, NY, 1994.

[19] G. Bachet, L. Chérigier, F. Doveil, Ion velocity distribution function observations in a multipolar argon discharge, Phys. Plasmas 2 (1995) 1782–1788.

[20] M.J. Goeckner, J. Goree, T.E. Sheridan, Measurements of ion velocity and density in the plasma sheath, Phys. Fluids B 4 (1992) 1663–1670.

[21] J.F. Clarke, M. McChesney, The Dynamics of Real Gases, Butterworths Scientific Publications, London, 1964 (Chapter 7).

[22] P.C. Stangeby, The plasma sheath, in: D.E. Post, R. Behrisch (Eds.), Physics of Plasma Wall Interactions in Controlled Fusion, Proc. NATO Advanced Study Institute, Val-Morin, Quebec, Canada, July 30–August 10, 1984, Plenum, NY, 1986, pp. 41–97.

[23] W.G. Vincenti, C.H. Kruger Jr., Introduction to Physical Gas Dynamics, Wiley, NY, 1970.

[24] S. Masuzaki, N. Ohno, S. Takamura, Experimental study on plasma heat flow to plasma-facing materials, J. Nucl. Mater. 223 (1995) 286–293.